

IVUS-Based Local Vessel Estimation for Robotic Intravascular Navigation

Beatriz Farola Barata^{1,2}, Phuong Toan Tran¹, Gianni Borghesan^{1,3}, Keir McCutcheon^{4,5}, Diego Dall'Alba², Paolo Fiorini², Jos Vander Sloten¹, and Emmanuel Vander Poorten¹

Abstract—Intra-operative local 3D vessel representations have the potential to significantly decrease the use of contrast agents and exposure to ionizing radiation during endovascular procedures, while overcoming the 2D visualization limitation of fluoroscopic guidance. By fusing intravascular ultrasound (IVUS) imaging and electromagnetic (EM) pose sensing in a robotic catheter tip, a real-time local 3D model of the vasculature could be constructed intra-operatively. This paper proposes the use of a cylinder model to approximate the vessel geometry near the catheter tip. An unscented Kalman filter is employed to robustly estimate the cylinder that best fits IVUS and EM data while navigating through the vessel. This forms a radiation-free alternative to conventional radiation-based guidance. Validation on one *in silico* and two *in vitro* models showed median estimation errors of cylinder radius of 0.14 mm, 0.42 mm and 0.70 mm; cylinder position of 0.45 mm, 1.07 mm and 0.96 mm; and cylinder orientation of 2.94°, 4.60° and 3.03° showing great potential for helping interventionists preventing harmful interactions between the instrument tip and the vessel wall.

Index Terms—Computer vision for medical robotics, navigation assistance, sensor fusion, 3D vessel modelling

I. INTRODUCTION

CARDIOVASCULAR diseases (CVDs) are the primary cause of death worldwide. In 2016 alone, the number of CVDs deaths was estimated at 17.9 million, representing 31% of all global deaths [1]. More specifically, in Europe, CVDs are responsible for the death of more than 4 million people yearly, accounting for 45% of all deaths [2]. Endovascular interventions are routinely used in the treatment of patients with CVDs. These are minimally invasive procedures with noted advantages, such as smaller incisions, short recovery

Manuscript received: February 23, 2021; Revised: April 28, 2021; Accepted: July 12, 2021.

This paper was recommended for publication by Editor Eric Marchand upon evaluation of the Associate Editor and Reviewers' comments. This work was supported by the ATLAS project. This project has received funding from the European Union's Horizon 2020 research and innovation programme under the Marie Skłodowska-Curie grant agreement No 813782. (B. Farola Barata and P. T. Tran contributed equally to this work.) (Corresponding author: B. Farola Barata.)

¹B. Farola Barata, P. T. Tran, G. Borghesan, J. Vander Sloten and E. Vander Poorten are with the Robot-Assisted Surgery Group, Department of Mechanical Engineering, KU Leuven, Belgium {beatriz.barata, phuongtoan.tran, gianni.borghesan, jos.vandersloten, emmanuel.vanderpoorten}@kuleuven.be

²B. Farola Barata, D. Dall'Alba and P. Fiorini are with the Altair Robotics Laboratory, Department of Computer Science Verona, University of Verona, Italy {diego.dallalba, paolo.fiorini}@univr.it

³G. Borghesan is also with Core Lab ROB, Flanders Make, Belgium

^{4,5}K. McCutcheon is with the Departments of Cardiovascular Medicine, University Hospitals Leuven, Belgium and with the Department of Cardiovascular Sciences, KU Leuven, Belgium keir.mccutcheon@uzleuven.be

Digital Object Identifier (DOI): see top of this page.

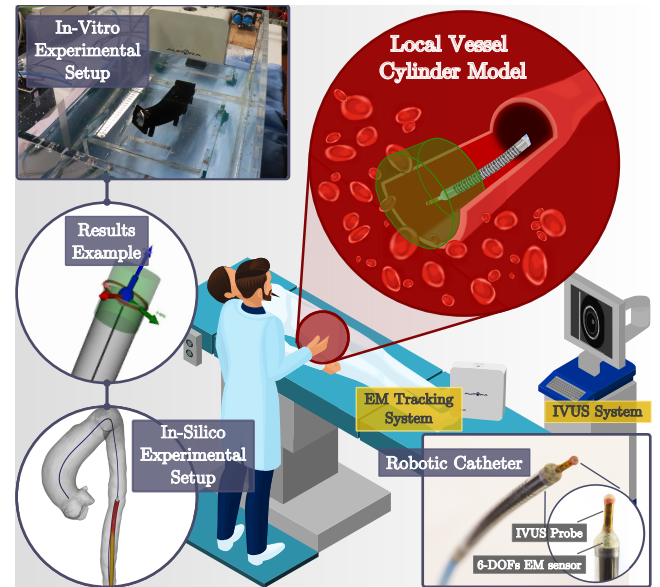


Fig. 1. Overview of a radiation-free guidance system for catheter navigation during endovascular interventions. Through fusion of EM tracking and IVUS-based vessel segmentation, a real-time 3D cylinder model that locally approximates the vessel geometry is proposed. Based on this knowledge, the catheter can be steered safely through the vessel.

time, and a decrease of blood loss and pain. Endovascular interventions are typically carried out using catheters, for which navigation is mostly achieved by manual manipulation at their proximal end, while resorting to various visual feedback tools [3]. Fluoroscopy is the most common imaging modality chosen for visualization during endovascular procedures. Based on X-rays, fluoroscopy is limited to a two-dimensional (2D) view of the surgical scene. Contrast agents are frequently injected to enhance the visualization of the instruments and blood vessels. Not only are contrast agents nephrotoxic, but also prolonged X-ray exposure is known to be harmful for both patient and clinician [3]. Since only 2D visual feedback is available, the clinician must continuously relate the 2D fluoroscopic images to a three-dimensional (3D) representation of the vasculature. In summary, he/she struggles with poor situational awareness, requiring 2D fluoroscopic images from different angles [3], [4]. This struggle combined with high procedural complexity can prompt undesired outcomes. Moreover, the inherent restricted access to the patient's anatomy demands an increased dexterity from the catheter operator to ensure safe navigation. External guidance imaging or robotics could improve navigation precision.

The addition of sensors and adoption of robotic approaches could effectively improve the operator's and/or the surgical robot's situational awareness and, ultimately, eliminate the need for fluoroscopy for localizing and navigating the instrument through the vasculature [5]. Various sensing modalities have been investigated in the literature to localize robotic instruments and/or to visualize the blood vessel. Examples of radiation-free sensing include intravascular ultrasound (IVUS) imaging [6] and electromagnetic (EM) pose sensing [7]. When embedded in robotic catheters, they allow for spatial localization of the catheter tip with respect to the surrounding vessel. EM sensors (pose in 6-degrees of freedom (DOFs)) are tracked and localized relative to an external coordinate system. An IVUS probe provides only local information of a vessel as it generates single cross-sectional ultrasound (US) images from within the vessel. Such characteristic largely complicates the direct use of this imaging modality as a path planning tool.

3D vessel models obtained from pre-operative imaging could potentially help gain insight into the patient anatomy. In fact, 3D reconstruction of blood vessels has been achieved by combining IVUS imaging with other sensing modalities such as angiography, pre-operative CT and EM tracking. Some examples are [8], [9], where angiographic projections are registered with IVUS to create a more detailed model of the vessel geometry. However, drawbacks of these methods remain: exposure to radiation (X-rays) and use of contrast agents, the common assumption of constant speed during catheter pullback, and the inaccurate estimation of the IVUS image axial orientation [6].

Recent developments including EM sensing have allowed for online registration as the catheter navigates through the vessel [10]. Registration of the EM measurements of the catheter tip to the pre-operative vessel geometry could in fact provide accurate spatial localization of IVUS images. However, in [10], the catheter must first advance deep into the vessel and intra-operative vessel deformation is not accounted for. Another relevant method [7] uses a Kalman filter to smooth the EM measurements and stitches consecutive IVUS images to reconstruct the vessel geometry. Even though this method does not rely on prior registration, it also does not provide any information regarding the vessel geometry ahead of the catheter. Another relevant framework is Simultaneous Catheter and Environment Modeling (SCEM) [11], which initially proposed to fuse IVUS and EM tracking to reconstruct blood vessels. SCEM was expanded to SCEM+ [12] introducing real-time 3D vessel reconstruction via a nonlinear optimization based on pre-operative data. The real-time operation of SCEM+ relies on the incorporation of pre-operative information and both SCEM and SCEM+ rely on accurate pre-registration between EM and CT data. Zhao *et al.* [13] introduces hereto a registration-free expansion to SCEM+, describing as well periodic vessel deformation from the cardiac cycle. Despite this progress, the latest version of SCEM+ still significantly depends on a static pre-operative geometry, which requires additional and avoidable contrast agent injection and exposure to ionizing radiation. Also, the reported vessel reconstruction errors are only determined after full catheter pullback and/or insertion. The vessel reconstruction accuracy and EM-CT

automatic registration performance are thus not evaluated over time (real-time operation).

In this paper, a reliable local 3D vasculature representation from local sensing (Fig. 1) is investigated and conceived to improve intra-operative catheter navigation and *in-situ* situational awareness, without relying on X-ray imaging, contrast agents and pre-operative data. A local cylinder model, updated at up to 40 Hz, is introduced as a simple geometry able to approximate important features of a blood vessel in the vicinity of the catheter tip. An estimation algorithm/module is proposed to infer the parameters of the cylinder in real-time solely by relying on IVUS images and EM tracking. An unscented Kalman filter (UKF) is implemented for estimating the best fitting cylinder model. Finally, the estimation algorithm and obtained local cylinder models are validated in both a simulation environment and in two blood vessel phantoms.

The paper is organized as follows: Section II gives an overview of the robotic catheter and the embedded sensors. Section III describes the cylinder model and its state space representations. Next, section IV introduces the proposed estimation algorithm (UKF). The experimental setup and simulation environment are reported in section V. The proposed approach validation results and discussion are included in section VI. Finally, in section VII, conclusions are drawn and directions for future work are given.

II. ROBOTIC CATHETER AND ITS IVUS AND EM SENSORS

Fig. 1 illustrates the hereby proposed cylinder model and its use in a clinical scenario. This work aims at facilitating a larger planning horizon to enhance catheter navigation, by providing a 3D model of the environment surrounding the catheter tip and by only using IVUS and EM sensing.

In order to gather the needed measurements from IVUS and EM tracking, a robotic catheter with a distal active segment was designed and built (see Fig. 1). The catheter has four McKibben muscles integrated, allowing bi-directional 2-DOFs bending over a bending segment of 80 mm at the distal tip. The design process and modelling of the robotic catheter's actuated segment are detailed in [14]. One EM Aurora sensor (Northern Digital Inc., Waterloo, Ontario, Canada) is embedded in the catheter at the steerable segment tip. Similarly, a single IVUS Visions PV .035 probe (Philips Healthcare, Andover, Massachusetts, USA) is located at the tip of the steerable segment. Note that the sensory data used in the estimation algorithm is relative to the robotic catheter tip.

A. EM and IVUS sensor measurements

When placed in a known electromagnetic field, the EM sensor 6-DOFs pose is measured and, consequently, the pose of the IVUS probe and the robotic catheter tip can be derived. The IVUS probe pose is represented by the homogeneous transformation matrix ${}_wT^i$, describing the pose of the IVUS frame $\{i\}$ in the world frame $\{w\}$. The IVUS probe pose is determined from the EM sensor pose ${}_wT^e$ and from the constant pose ${}_eT^i$ of the IVUS probe relative to the EM sensor (known by the catheter design). Similarly, one can compute the pose of the catheter tip with respect to the world frame $\{w\}$

${}_w\mathbf{T}^{tip}$, also with a fixed transformation matrix ${}_e\mathbf{T}^{tip}$ known from catheter design. These relations are summarized as:

$${}_w\mathbf{T}^i = {}_w\mathbf{T}^e {}_e\mathbf{T}^i \quad (1)$$

$${}_w\mathbf{T}^{tip} = {}_w\mathbf{T}^e {}_e\mathbf{T}^{tip} \quad (2)$$

Standard registration techniques can be adopted to derive ${}_e\mathbf{T}^i$ and ${}_e\mathbf{T}^{tip}$, while ${}_w\mathbf{T}^e$ is measured by the EM system.

The IVUS measurements show a cross-sectional 2D US view of the vessel at the level of the IVUS probe. Since this sensor is aligned with the longitudinal axis of the catheter, the cross-section is thus perpendicular to this longitudinal axis and is visible in the xy -plane of the IVUS frame $\{i\}$, rigidly attached to the center of the IVUS probe (see Fig. 1 and 2). The contour of the vessel lumen can be extracted from the IVUS slice and is represented by a set of M consecutive 2D points ${}_i^j\mathbf{c}$ spaced every $\frac{2\pi}{M-1}$ radians:

$${}_i^j\mathbf{c} = [{}_i^jc_x \quad {}_i^jc_y]^T \quad (j = 1, \dots, M) \quad (3)$$

In this work, as described in [7], a stable and automatic method is adopted to extract the vessel lumen contour from the IVUS images and consequently the points described in (3).

III. CYLINDER MODELLING

The vessel geometry is locally approximated with a cylinder of infinite height, in the vicinity of the catheter tip. This cylinder is characterized by a 5-dimensional state vector including the cylinder radius r and the cylinder pose, which consists of a 2-DOFs position and a 2-DOFs orientation. It is important to note that both the position and the orientation of the cylinder model are expressed in the IVUS frame $\{i\}$ (Fig. 2). While the position vector ${}_i\mathbf{p}$ is defined so that it always lies on the xy plane of frame $\{i\}$, the orientation of the cylinder (2-DOFs) can be defined either by a unit vector ${}_i\mathbf{d}$ or by a pair of angles (θ, ϕ) . These two possible representations express the non-minimal (4) and the minimal (5) representations of the cylinder state, respectively, as in:

$$\begin{aligned} \mathbf{x}_{(i\mathbf{d})} &= [{}_i\mathbf{p}^T \quad {}_i\mathbf{d}^T \quad r]^T \\ &= [{}_ip_x \quad {}ip_y \quad {}id_x \quad {}id_y \quad {}id_z \quad r]^T \end{aligned} \quad (4)$$

$$\begin{aligned} \mathbf{x}_{(\theta, \phi)} &= [{}_i\mathbf{p}^T \quad \theta \quad \phi \quad r]^T \\ &= [{}_ip_x \quad {}ip_y \quad \theta \quad \phi \quad r]^T \end{aligned} \quad (5)$$

where $\theta \in [0, \pi]$ and $\phi \in [0, 2\pi]$.

When the cylinder state is encoded by the non-minimal representation ${}_i\mathbf{d}$, this is a singularity-free representation. However, a constraint on the state is introduced, which mathematical operations must respect. Alternatively, the minimal representation (θ, ϕ) is free of constraints and mathematical operations are easier to formulate. However, a singularity is intrinsically associated when the catheter tip is aligned with the longitudinal axis of the vessel ($\theta = 0^\circ$). In order to limit the occurrence of singularities, the range of θ and ϕ can be conveniently defined so that $\theta = 0^\circ$ is as far as possible from the nominal cylinder pose. The nominal cylinder pose is defined so the IVUS longitudinal z axis is parallel to the cylinder axis for $\theta = 90^\circ$ and $\phi = 90^\circ$. Fig. 2 illustrates how

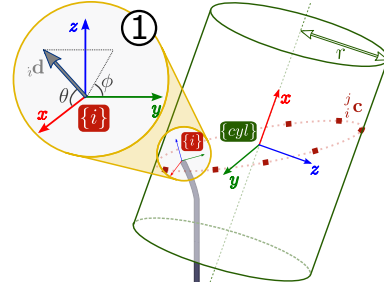


Fig. 2. Cylinder representation in the 6-DOFs frame $\{cyl\}$, in which the x axis corresponds to the direction ${}_i\mathbf{d}$ in the IVUS frame $\{i\}$. The cylinder 2-DOFs orientation can be represented in $\{i\}$ either by a unit vector ${}_i\mathbf{d}$ or by a pair of angles $\theta \in [0, \pi]$ and $\phi \in [0, 2\pi]$.

the orientation of the cylinder is described by the minimal and the non-minimal representations. The same figure shows how a 6-DOFs frame $\{cyl\}$ attached to the cylinder, and expressed with respect to $\{i\}$, is defined even though its pose retains 4-DOFs. The pose ${}_i\mathbf{T}^{cyl}$ of the frame $\{cyl\}$ expressed in frame $\{i\}$ is given by:

$${}_i\mathbf{T}^{cyl} = [{}_i\mathbf{R}^{cyl} \quad {}_i\mathbf{t}^{cyl}] = \begin{bmatrix} \cos \theta & -\sin \theta & 0 & {}ip_x \\ \sin \theta \cos \phi & \cos \theta \cos \phi & -\sin \phi & {}ip_y \\ \sin \theta \sin \phi & \cos \theta \sin \phi & \cos \phi & 0 \\ 0 & 0 & 0 & 1 \end{bmatrix} \quad (6)$$

Depending on the application, one state representation can be chosen over the other, which is further discussed in section IV, alongside with the need for frame $\{cyl\}$. Note that both state representations are related as follows:

$${}_i\mathbf{d} = \begin{bmatrix} {}id_x \\ {}id_y \\ {}id_z \end{bmatrix} = \begin{bmatrix} \cos \theta \\ \sin \theta \cos \phi \\ \sin \theta \sin \phi \end{bmatrix} \quad (7)$$

$$\theta = \arccos({}_id_x), \quad \phi = \text{atan2}({}_id_z, {}id_y) \quad (8)$$

It is noteworthy that the aforementioned cylinder state representations cannot be directly observed from the EM and IVUS sensor measurements. In this paper, the state is inferred from a plurality of subsequent sensor measurements, while taking into account the noise of the IVUS and EM measurements and the uncertainty of the system evolution over time. Further note that due to the axial symmetry inherent to using a cylinder model, IVUS measurements can be ambiguous, as illustrated in Fig. 3. Consequently, this ambiguity largely complicates the cylinder orientation estimation.

Lastly, it is important to discuss the consequences of the presence of side branches and bifurcations. These locally distort the axisymmetric geometry of the vessel and so, close to these sites, locally approximating the vessel by a cylinder model becomes less valid. Despite future work being planned to address local modeling at vessel bifurcation, in this work, the problem is simplified by closing the side-branches and bifurcations both in the *in-silico* and in the *in-vitro* experiments, by means of the employed image segmentation method.

IV. ONLINE LOCAL VESSEL ESTIMATION

In order to estimate the state of the proposed cylinder model, a specific implementation of recursive Bayesian filtering is

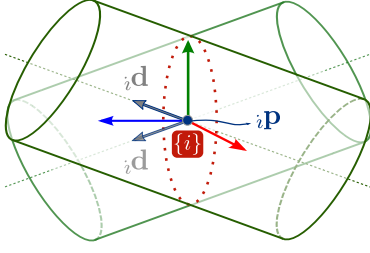


Fig. 3. Example of IVUS measurements ambiguity: two cylinders with identical radius r , position ${}_i\mathbf{p}$ and vessel lumen contours, but with distinct orientation ${}_i\mathbf{d}$ (a 180° rotation about the z axis of IVUS frame $\{i\}$).

investigated: the unscented Kalman filter (UKF), based on the scaled unscented transform with additive process and measurement noise. Hence, local vessel estimation occurs recursively over time while accounting for the noise and uncertainty of the system measurements and the system evolution, respectively. The UKF is a known extension to the Kalman filter, with a fast computation time and mainly designed to address nonlinear state transition and observation functions. Yet, since only the mean and covariance of the posterior distribution are propagated, while presuming consistent estimates of the state probability density function, the following are assumed to be Gaussian: *i*) the posterior probability density function $p(\mathbf{x}_k|\mathbf{z}_{1:k}, \mathbf{u}_{1:k})$, *ii*) the state transition density $p(\mathbf{x}_k|\mathbf{x}_{k-1})$, *iii*) the observation likelihood $p(\mathbf{z}_k|\mathbf{x}_k)$, *iv*) the process noise probability density function $p(\mathbf{v}_k)$, and *v*) the measurement noise probability density function $p(\mathbf{n}_k)$.

In order to estimate the vessel geometry, the state and covariance representation must be identified first. To this regard, it is important to recall that, as introduced in section III, the cylinder state can be represented by the non-minimal $\mathbf{x}_{(i,d)}$ or the minimal $\mathbf{x}_{(\theta,\phi)}$ representations. These present different characteristics which are exploited in our method. This is, while $\mathbf{x}_{(\theta,\phi)}$ is used to represent the cylinder state throughout the different steps of the implemented UKF, the alternate representation $\mathbf{x}_{(i,d)}$ is best used to formulate the state transition function $\mathbf{f}(\cdot)$ and the observation function $\mathbf{h}(\cdot)$. The latter stems from the fact that a representation free of singularities is preferred when operating with homogeneous transformation matrices as it is the case with $\mathbf{f}(\cdot)$ and $\mathbf{h}(\cdot)$. Therefore, conversion between the two representations is deemed necessary before and after applying the state transition and observation functions. The state uncertainty is represented by a (5×5) covariance matrix.

The recursion for vessel estimation by means of the UKF starts from the posterior probability density function $p(\mathbf{x}_{k-1}|\mathbf{z}_{1:k-1}, \mathbf{u}_{1:k-1})$ at time $k-1$, generally described by:

$$p(\mathbf{x}_{k-1}|\mathbf{z}_{1:k-1}, \mathbf{u}_{1:k-1}) = \mathcal{N}(\mathbf{x}_{k-1}; \hat{\mathbf{x}}_{k-1}, \mathbf{P}_{\hat{\mathbf{x}}_{k-1}}) \quad (9)$$

where $\mathcal{N}(\mathbf{x}_{k-1}; \hat{\mathbf{x}}_{k-1}, \mathbf{P}_{\hat{\mathbf{x}}_{k-1}})$ is the multivariate Gaussian probability density function, evaluated at point \mathbf{x}_{k-1} at time $k-1$, of mean $\hat{\mathbf{x}}_{k-1}$, the estimated mean state, and corresponding covariance matrix $\mathbf{P}_{\hat{\mathbf{x}}_{k-1}}$.

By employing the scaled unscented transform, $p(\mathbf{x}_{k-1}|\mathbf{z}_{1:k-1}, \mathbf{u}_{1:k-1})$ (9) is approximated by a set of weighted sigma points \mathcal{X}_i which are then passed through the

nonlinear state transition function $\mathbf{f}(\cdot)$, resulting in a set of transformed points, the predicted states $\tilde{\mathcal{X}}_i$:

$$\tilde{\mathcal{X}}_i = \mathbf{f}(\mathcal{X}_i, \mathbf{u}_k, \mathbf{v}_k) \quad \text{for } i = 1, \dots, N_{\mathcal{X}} \quad (10)$$

with \mathbf{u}_k and \mathbf{v}_k being generally described as a known external input and the process noise of the system, respectively.

In the case at hand, the EM measurements obtained from the EM sensor form the inputs to the state transition function. Their uncertainty is thus expressed in the process noise of the system. The radius and pose of the cylinder model are, over time, assumed constant relative to the world coordinate frame $\{w\}$. This stems from the fact that the cylinder approximation of the vessel is being locally estimated in the vicinity of the catheter tip. Yet, unmodelled physiological dynamic effects, such as the heartbeat and breathing motion, possibly entail small variations to this assumption.

Furthermore, one must keep in mind that, considering the cylinder state representations, the cylinder pose is expressed in the IVUS frame $\{i\}$ (see (4) and (5)). Therefore, a displacement of the catheter tip will consequently affect the cylinder state. Between time instances $k-1$ and k , changes in the cylinder state (variations in the catheter tip pose) are thus determined from the EM measurements via the displacement of the EM frame, represented by the homogeneous transformation matrix ${}_{e_k}\mathbf{T}^{e_{k-1}}$ between the EM frame $\{e\}$ at time k and the EM frame $\{e\}$ at time $k-1$:

$${}_{e_k}\mathbf{T}^{e_{k-1}} = {}_{e_k}\mathbf{T}^w {}_w\mathbf{T}^{e_{k-1}} \quad (11)$$

Accordingly, the displacement of the IVUS frame $\{i\}$, attached to the IVUS probe, between the time instants $k-1$ and k is described by:

$${}_{i_k}\mathbf{T}^{i_{k-1}} = {}_i\mathbf{T}^e {}_{e_k}\mathbf{T}^w {}_w\mathbf{T}^{e_{k-1}} {}_{e_{k-1}}\mathbf{T}^i = \begin{bmatrix} {}_{i_k}\mathbf{R}^{i_{k-1}} & {}_{i_k}\mathbf{t}^{i_{k-1}} \\ \mathbf{0}_{1 \times 3} & 1 \end{bmatrix} \quad (12)$$

where ${}_{i_k}\mathbf{R}^{i_{k-1}}$ and ${}_{i_k}\mathbf{t}^{i_{k-1}}$ describe, respectively, the rotation matrix and the translation vector of the homogeneous transformation matrix ${}_{i_k}\mathbf{T}^{i_{k-1}}$ between the IVUS frame $\{i\}$ at time k and the IVUS frame $\{i\}$ at time $k-1$.

Considering the variation of the IVUS frame pose between the time instances $k-1$ and k , the direction and the position of the cylinder model at time $k-1$ are expressed in the new frame $\{i\}_k$ by the following:

$${}_{i_k}\mathbf{d} = {}_{i_k}\mathbf{R}^{i_{k-1}} {}_{i_{k-1}}\mathbf{d} \quad (13)$$

$${}_{i_k}\mathbf{p} = \mathbf{f}_p({}_{i_k}\mathbf{R}^{i_{k-1}} {}_{i_{k-1}}\mathbf{p} + {}_{i_k}\mathbf{t}^{i_{k-1}}) \quad (14)$$

with $\mathbf{f}_p(\cdot)$, the function projecting the cylinder position in the xy plane of frame $\{i\}_k$ along the direction ${}_{i_k}\mathbf{d}$ (see Fig. 4). By projecting it, the cylinder position will be kept in the vicinity of the catheter tip as the cylinder model is assumed of infinite length along its longitudinal direction.

In a nutshell, the state transition function considers ${}_{i_k}\mathbf{p}$ (14), the angles (θ_k, ϕ_k) calculated from ${}_{i_k}\mathbf{d}$ (13) by means of cylinder state representations conversion (8), and r_{k-1} , the cylinder radius at time $k-1$:

$$\mathbf{f}(\mathbf{x}_{k-1}, \mathbf{u}_k) = [{}_{i_k}\mathbf{p}^T \quad \theta_k \quad \phi_k \quad r_{k-1}]^T \quad (15)$$

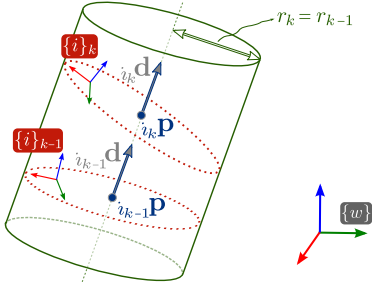


Fig. 4. Cylinder pose evolution, between time instants $k-1$ and k , considering a variable IVUS frame $\{i\}$: the cylinder radius r and its pose expressed in the world frame $\{w\}$ are assumed constant over time.

where, as abovementioned, the input \mathbf{u}_k consists of the EM displacement ${}^e_k \mathbf{T}^{e_{k-1}}$ (see (11)).

Represented by a (5×5) diagonal covariance matrix, the process noise is assumed to be normally distributed with zero mean, additive and independent. Also, it is presumed constant over time for any state variable of $\mathbf{x}_{(\theta, \phi)}$ (5), besides the angle ϕ . The related process noise of ϕ is conditioned to the current estimated value of θ (since θ true value is unknown), so no specific orientation θ or ϕ is preferred by the process noise:

$$\sigma_\phi^2 = \frac{\sigma_\theta^2}{\sin^2 \theta} \quad (16)$$

with σ_θ^2 and σ_ϕ^2 , the variances on θ and on ϕ , respectively.

From (10), the mean predicted state $\tilde{\mathbf{x}}_k$ and covariance $\mathbf{P}_{\tilde{\mathbf{x}}_k}$ for the current time k are obtained from the predicted states $\tilde{\mathcal{X}}_i$ (transformed sigma points) weighted average and covariance. The prediction of the current state \mathbf{x}_k considering the previous state \mathbf{x}_{k-1} , current inputs $\mathbf{u}_{1:k}$ and previous measurements $\mathbf{z}_{1:k-1}$ is generally formulated as follows:

$$p(\mathbf{x}_k | \mathbf{z}_{1:k-1}, \mathbf{u}_{1:k}) = \mathcal{N}(\mathbf{x}_k; \tilde{\mathbf{x}}_k, \mathbf{P}_{\tilde{\mathbf{x}}_k}) \quad (17)$$

The prediction $\tilde{\mathbf{x}}_k$ is updated with the current measurement \mathbf{z}_k by again resorting to the scaled unscented transform, in which a new set of sigma points $\tilde{\mathcal{X}}_i^*$ approximates the probability density function describing the prediction equation (17). The new set of transformed points, here the predicted measurements $\tilde{\mathbf{z}}_k$, results from passing the new set of sigma points $\tilde{\mathcal{X}}_i^*$ through the observation function:

$$\tilde{\mathbf{z}}_i = \mathbf{h}(\tilde{\mathcal{X}}_i^*, \mathbf{n}_k) \quad \text{for } i = 1, \dots, N_{\mathcal{X}} \quad (18)$$

with \mathbf{n}_k being the measurement noise.

This work includes solely IVUS data in the measurement vector \mathbf{z}_k . In particular, this vector encompasses the distances between the origin of frame $\{i\}$ to each point ${}^j_i \mathbf{c}$. Each point ${}^j_i \mathbf{c}$ is comprised of a series of M points ${}^j_i \mathbf{c}$ ($j = 1, \dots, M$) evenly spaced every $\frac{2\pi}{M-1}$ radians and determined for each IVUS image over the contour of the vessel lumen. It should be noted that the lumen contour lies in the xy plane of the IVUS frame $\{i\}$. Considering the abovementioned and that $\|\cdot\|$ describes the 2-norm of the respective vectors, the measurement vector \mathbf{z}_k is given by:

$$\mathbf{z}_k = [\|{}^1_i \mathbf{c}\| \quad \|{}^2_i \mathbf{c}\| \quad \dots \quad \|{}^M_i \mathbf{c}\|]^T \quad (19)$$

Furthermore, each element of the measurement vector \mathbf{z}_k has an associated measurement noise. This is represented by an $(M \times M)$ diagonal covariance matrix. Analogous to the process noise, this matrix is assumed to be normally distributed with zero mean, additive, independent and constant over time.

The output vector of the observation function includes the distances from a series of M points ${}^j_i \mathbf{c}$ ($j = 1, \dots, M = 4$) evenly spaced every $\frac{2\pi}{M-1}$ radians, to the origin of $\{i\}$. These points are sampled from the contour that is obtained from the intersection of the cylinder, represented by the state vector \mathbf{x}_k , with the xy plane of the IVUS frame $\{i\}$. By simulating the generation process of actual IVUS measurements, the observation function $\mathbf{h}(\mathbf{x}_k)$ is obtained:

$$\mathbf{h}(\mathbf{x}_k) = [\|{}^1_i \tilde{\mathbf{c}}\| \quad \|{}^2_i \tilde{\mathbf{c}}\| \quad \dots \quad \|{}^M_i \tilde{\mathbf{c}}\|]^T \quad (20)$$

Besides, given that the state vector \mathbf{x}_k of the cylinder model intersects the xy plane of the IVUS frame $\{i\}$ to compose the observation function, the origin of frame $\{i\}$ must be bounded to stay within the cylinder as the catheter is expected to stay inside the vessel (see Fig. 5):

$$\|{}_{cyl} \mathbf{t}^{i_k}\| = \left\| - \left({}_{i_k} \mathbf{R}^{cyl} \right)^T {}_{i_k} \mathbf{t}^{cyl} \right\| \leq r_k \quad (21)$$

where ${}_{i_k} \mathbf{R}^{cyl}$ and ${}_{i_k} \mathbf{t}^{cyl}$ compose the pose ${}_{i_k} \mathbf{T}^{cyl}$ of the frame $\{cyl\}$, attached to the cylinder model, expressed in the frame $\{i\}$. This relation is better described in section III (see (6) and Fig. 2). Note that when the sigma points do not satisfy (21) (the constraint), the output of the observation function is adapted as illustrated in Fig. 5, since the origin of frame $\{i\}$ falls outside the predicted cylinder. From this, the estimation error of the UKF is anticipated to increase and so, it is necessary to handle such case.

Following up from (18), the mean predicted measurement $\tilde{\mathbf{z}}_k$ and covariance $\mathbf{P}_{\tilde{\mathbf{z}}_k}$ are obtained from the weighted average and covariance of $\tilde{\mathcal{Z}}_i$. From the difference between the predicted measurements $\tilde{\mathbf{z}}_k$ and the actual measurements \mathbf{z}_k , by means of the Kalman gain $\mathbf{K} = \mathbf{P}_{\tilde{\mathbf{x}}_k \tilde{\mathbf{z}}_k} \mathbf{P}_{\tilde{\mathbf{z}}_k}^{-1}$, the updated state $\hat{\mathbf{x}}_k$ and its corresponding covariance $\mathbf{P}_{\hat{\mathbf{x}}_k}$ are determined:

$$\hat{\mathbf{x}}_k = \tilde{\mathbf{x}}_k + \mathbf{K}(\mathbf{z}_k - \tilde{\mathbf{z}}_k) \quad (22)$$

$$\mathbf{P}_{\hat{\mathbf{x}}_k} = \mathbf{P}_{\tilde{\mathbf{x}}_k} - \mathbf{K} \mathbf{P}_{\tilde{\mathbf{z}}_k} \mathbf{K}^T \quad (23)$$

where $\mathbf{P}_{\tilde{\mathbf{x}}_k \tilde{\mathbf{z}}_k}$ is the weighted cross-covariance of $\tilde{\mathbf{x}}_k$ and $\tilde{\mathbf{z}}_k$.

Finally, the prediction is updated as follows:

$$p(\mathbf{x}_k | \mathbf{z}_{1:k}, \mathbf{u}_{1:k}) = \mathcal{N}(\mathbf{x}_k; \hat{\mathbf{x}}_k, \mathbf{P}_{\hat{\mathbf{x}}_k}) \quad (24)$$

Note that equation (24) formulates the general equation (related to the prediction update) characteristic to the UKF.

V. EXPERIMENTAL SETUP AND VALIDATION METRICS

In this section, the experimental setups used to validate and further demonstrate the proposed methods are described. Validation took place in a catheter-based simulation environment [15] (*in silico* experiments) using synthetic sensor measurements, and in two simple blood vessel phantoms (*in vitro* experiments), in which the robotic catheter was steered. Fig. 1 shows both the simulation environment and the vessel phantoms setup, also visible in Fig. 6. Altogether,

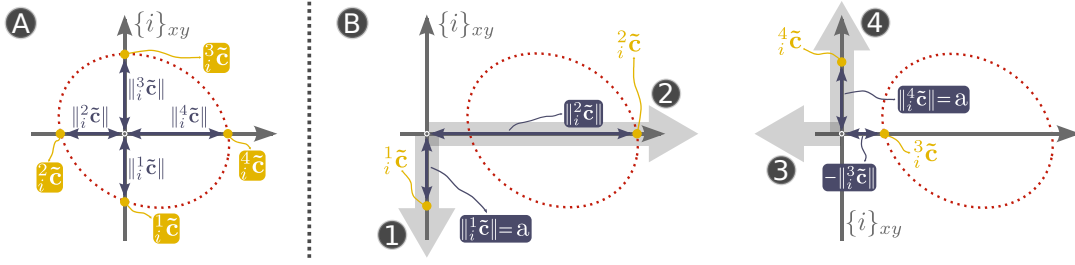


Fig. 5. Representation of the origin of $\{i\}$ (A) within the predicted cylinder (the sampled contour points can be directly computed at the different intersections) and (B) falling outside the predicted cylinder. For the latter, a radial scanning direction (\Rightarrow) defines different cases: When no intersection takes place (①, ④), a constant distance a is used to define the contour points. When intersections reside in the same direction (②, ③), both intersection points are used.

20 experiments were conducted *in silico* and, subsequently, one experiment per the two vessel phantoms was performed *in vitro*. The estimation errors of the cylinder position, radius and orientation with respect to the ground-truth geometric data were used for assessing the estimation method. The ground-truth data was obtained by fitting 10 mm long cylinders along the vessel geometry surrounding the catheter tip. From this, the error between the estimated cylinder models state and the respective vessel section ground-truth cylinders state was directly calculated at each simulation or time step. Moreover, the validity of the proposed local cylinder model, used as the ground-truth cylinders, was evaluated across the entire length of a modified/closed patient-specific aortic model (see Fig. 1). The UKF was implemented in Python and all the experiments ran on an Intel Core i7-8850H (2.60 GHz).

A. In silico experimental setup

The main components of the simulation environment were the following: (1) a patient-specific aortic model, (2) synthetically generated EM and IVUS data, and (3) a simulated virtual catheter. The patient-specific aortic model, provided by UZ Leuven, was derived from segmented CT scans of a patient's aorta: in the context of this work, all side-branches in the model were artificially closed. For realistic synthetic data, EM noise was added and modelled by Gaussian noise with a zero mean and a standard deviation of 0.3 mm and 0.5° for the translational and rotational parts of the twist, respectively. Similarly, Gaussian noise with a zero mean and a standard deviation of 1 mm was added to the coordinates of the synthetic IVUS data. This data is given in the form of IVUS contour points $\tilde{\mathbf{c}}_j$ ($j = 1, \dots, M$), obtained by intersecting the xy -plane of the IVUS frame $\{i\}$ with the aortic model mesh (see Fig. 1). It is important to note that, while the EM system provides measurements at 40Hz, the frame grabber used for the IVUS image acquisition works at 12 frames per second (fps). As a result, the simulation was run at 12 fps. The simulated virtual catheter, whose pose is computed following an energy-minimization argumentation, is described in [15]. During the *in silico* experiments, the catheter was commanded to repeatedly follow a pre-defined trajectory along the vessel in order to better assess the UKF performance during catheter insertion or bending. This pre-defined trajectory consisted of a forward translation of 20 mm at 2.4 mm/s and a series of

bending commands at 4.8 °/s: 30° bending of the catheter tip in a single bending plane (BP), 360° bending of the BP and -30° bending of the catheter tip in the original BP.

B. In vitro experimental setup

Experiments conducted in the vessel phantoms were carried out with the robotic catheter from section II. At each time step, a local cylinder model was estimated. During these experiments, catheter navigation consisted of repeating (1) manual insertion of various length, (2) 38° of catheter tip bend in a single BP, (3) 360° catheter tip bend of the BP, and (4) -38° catheter tip bend in the first single BP. Bending occurred at 3.6 °/s, whilst insertion was performed at approximately 1.5 mm/s. Ultrasound compatible Agar-Agar vessel mock-ups, consisting of a solution of de-ionized water with 5wt% of 900 g/cm² dry agar powder were used. The phantoms were designed and built in-house, offering simple representations of vessels with fixed (16 mm) and variable (from 8 to 10 mm) inner radius. They, therefore, do not mimic a specific section of a patient's vasculature. The experiments were carried out in de-ionized water, facilitating IVUS ultrasound wave propagation, and the mock-ups were registered such that their ground-truth for the cylinder estimation validation was available.

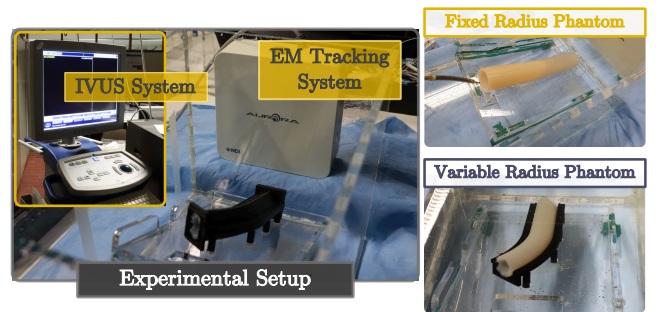


Fig. 6. Depiction of the experimental setup and of the two vessel phantoms' exterior used in the *in-vitro* validation.

VI. RESULTS AND DISCUSSION

The validity to capture the main features of a blood vessel by a cylinder was determined in the simulation environment by fitting 10 mm long cylinders to various sections of the simulated aorta. The quality of the fit was assessed by calculating, at each simulation step, the distance between the fitted

cylinder and the nodes of the corresponding vessel section. Overall, for the entire vessel length, a median fitting error of 0.35 mm was found (Fig. 7 (B)). Considering that the aortic model radius is approx. 10 mm, the obtained small fitting errors median validate the earlier assumption that 10 mm long cylinders are enough to capture the main local geometric characteristics of the vessel. Moreover, given that the cylinder is continuously updated, the model was deemed sufficient for providing meaningful navigation assistance. Such conclusion is also supported by the consistency of the fitting errors along the closed aortic model with an interquartile range (IQR) of just 0.39 mm (Q1 of 0.16 mm; Q3 of 0.55 mm).

Conversely, in a supplementary analysis conducted solely to further check the cylinder assumption, as demonstrated in Fig. 7 (A), the fitting errors distribution of an aorta with side-branches shows larger median (0.49 mm) and IQR (0.99 mm) values compared to a closed aorta. This increase is prompted by the presence of side-branches, as depicted in the 3D colored error map of Fig. 7 (left). Around these areas (at the proximal aorta and at the aortic arch), the axisymmetric geometry of the vessel is locally distorted and so, errors relative to the fitted cylinders increase. Side-branches lead to not only larger variability, but also a longer right tail, giving a Q3 of 1.20 mm and a Q1 of 0.21 mm. It should be stressed that the results in this work do not account for the geometric distortions occurring in the vicinity of a side-branch. That is, in this framework, while the vessel involved in the ongoing catheter navigation (main vessel) is modelled by the proposed cylinder, side-branches are not. When the catheter does not need to branch out from such main vessel, the proposed cylinder model is thus useful.

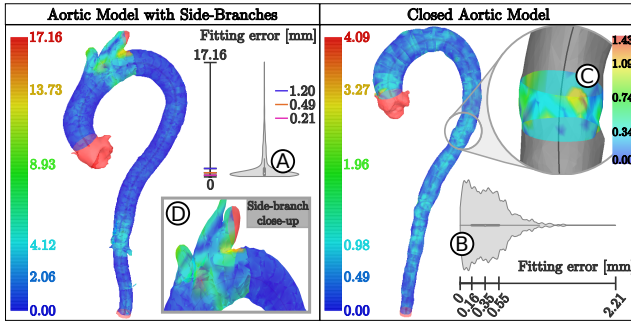


Fig. 7. Fitting errors (values in colorbars) representations and distributions of 10 mm long cylinders in an aorta with side-branches (left, (A)) and a closed aorta (right, (B)). An example of a fitted cylinder (C) of the closed aorta is shown with corresponding errors. As portrayed in the side-branch close-up (D), a cylinder model would have too large errors (4 – 5 mm) to adequately model side-branches.

For all the experiments, the initial state \mathbf{x}_0 , the initial diagonal covariance matrix $\mathbf{P}_{\mathbf{x}_0}$, the process noise covariance matrix $\mathbf{P}_{\mathbf{v}_k}$, the measurement noise ($M = 10$) covariance matrix $\mathbf{P}_{\mathbf{n}_k}$ and the scaling parameters from the scaled unscented transform κ , α and β were set as summarized in Table I.

In order to better handle the earlier mentioned ambiguous nature of the IVUS measurements (Fig. 3), the measurement noise was selected higher than the process noise. This relation between measurement and process noises means an increased

TABLE I
UKF PARAMETERS USED IN BOTH THE *in silico* AND *in vitro* EXPERIMENTS

\mathbf{x}_0	$[0 \text{ mm} \ 0 \text{ mm} \ \frac{\pi}{2} \ \frac{\pi}{2} \ 15 \text{ mm}]$
$\mathbf{P}_{\mathbf{x}_0}$	$\text{diag}([5 \text{ mm} \ 5 \text{ mm} \ \frac{\pi}{12} \ \frac{\pi}{12} \ 5 \text{ mm}])^2$
$\mathbf{P}_{\mathbf{v}_k}$	$\text{diag}([0.01 \text{ mm} \ 0.01 \text{ mm} \ \frac{\pi}{3600} \ \frac{\pi}{3600} \ 0.5 \text{ mm}])^2$
$\mathbf{P}_{\mathbf{n}_k}$	$\text{diag}([3.5 \text{ mm} \ \dots \ 3.5 \text{ mm}])^2$
$[\kappa \ \alpha \ \beta]$	$[0 \ 1 \ 2]$

confidence in the state transition function and the EM input (which are not multimodal) and a reduced confidence in the IVUS measurements. This then conditions the UKF to more likely infer the correct cylinder state. Note that the IVUS ambiguity mainly influences the orientation estimation, in particular during catheter tip insertion with no bending, as it creates multiple modes to which the filter is susceptible to converge. When solely inserting the catheter, consecutive IVUS images will show little change and, if the probe is parallel to the vessel local centerline, the orientation uncertainty will increase. In these cases, the filter may not converge to the correct mode. Active catheter tip bending is thus beneficial to duly infer the cylinder state.

The *in silico* validation comprised 20 simulated trials, during which the cylinder radius and position were accurately estimated. Both cylinder state parameters converged to the correct mode after a few recursion steps of the UKF. This is visible in Fig. 8 (A), where the evolution of the estimation errors of one trial is depicted. Over the 20 conducted trials, the radius and position errors median and IQR were 0.14 mm and 0.17 mm and 0.45 mm and 0.36 mm, respectively (Fig. 8 (B)). Besides an accurate estimation of the cylinder radius and position, the small IQRs demonstrate low estimation variability. These results suggest consistency in the estimation and the robustness and reliability of the proposed framework. On the other hand, the estimation of the cylinder orientation bears larger errors overall. With a median of 2.94° and an IQR of 1.90° (Fig. 8 (B)), the error is still acceptable. Furthermore, a growing value of the orientation uncertainty can be used as a trigger to actively bend the catheter and improve estimation accuracy. This follows from observing Fig. 8, where the orientation error diminishes during instants when the catheter is actively bent, while it rises during straight insertions. Nonetheless, the

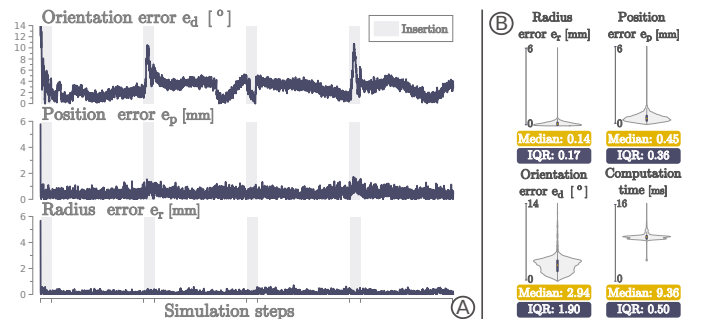


Fig. 8. Cylinder state estimation error progression of one simulated trial (A) and error distribution of the 20 simulated trials (B).

reproducibility of these results (from the small IQR) indicates a robust estimation of the local cylinder orientation. Also in Fig. 8 (A), note that the large errors visible at the start of the experiment occur because the UKF firstly considers the initial state \mathbf{x}_0 for the cylinder state estimation. Only after the initial recursion steps, as multiple measurements of the environment are taken into account by the filter, the algorithm correctly converges. This translates in a decrease of the cylinder state estimation errors. Finally, the computation time for one UKF recursion shows a median and IQR of respectively 9.36 ms and 0.50 ms, confirming the possibility of using the proposed method intra-operatively.

Regarding the *in vitro* validation, the cylinder radius (with median error: 0.42 mm and 0.70 mm; IQR of errors: 0.53 mm and 0.70 mm) and position (median error: 1.07 mm and 0.96 mm; IQR of errors: 0.95 mm and 0.70 mm) were accurately and precisely estimated, regardless of the vessel mock-up. The orientation estimation showed larger errors and oscillations (median errors: 4.69° and 3.03°; IQR of errors: 7.28° and 3.85°) compared to the simulated trials. Fig. 9 shows the error distribution of these results, alongside the error progression for the two conducted experiments (color-coded per phantom). Conversely to the *in silico* trials, during the *in vitro* experiments' probing phases (zones not highlighted in Fig. 9 plots), one can observe that local errors occasionally increase, especially the orientation error in the mock-up with variable inner diameter. These phenomena are expected to be caused by poor EM pose tracking, but also imperfect lumen segmentation and/or inaccuracies during the registration to the ground-truth cylinders. These factors together with straight insertion phases also strongly affect the orientation error dispersion prompting the verified higher orientation IQR values compared to the simulated trials. Nonetheless, the orientation estimation uncertainty can be used in the catheter navigation decision-making (e.g. to start bending), since this framework provides not only a local 3D model of the vasculature but also its current positioning relative to the catheter tip.

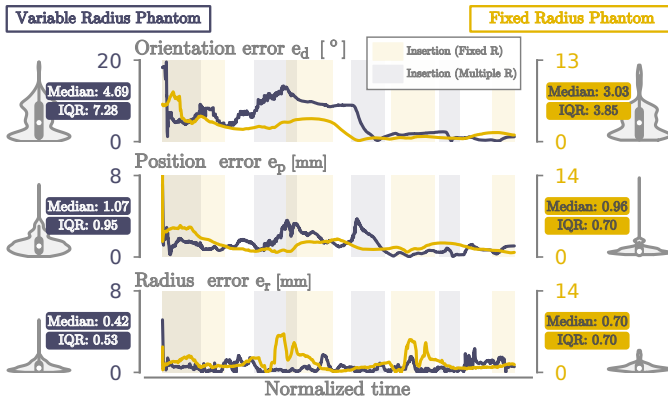


Fig. 9. Estimation errors progression of the two *in vitro* experiments conducted in a curved cylindrical variable radius phantom (blue) and a straight cylindrical fixed radius phantom (yellow).

VII. CONCLUSION AND FUTURE WORK

In this paper, we propose a method to support the navigation of robotic catheters relying only on non-ionizing sensing

modalities: EM tracking and IVUS imaging. The proposed approach could radically reduce the dependence on X-ray imaging, while still offering a way to steer the catheter in a more deliberate manner through the vessel, e.g. to avoid unintentional contact of the typically acute catheter tip with the fragile vessel. Moreover, the proposed method approximates the blood vessel geometry by a local cylinder model that can be estimated intra-operatively based on the aforementioned radiation-free sensing. This cylinder model offers an accurate and larger planning horizon ahead of the instrument tip, thus enhancing decision-making and forming a first step to autonomous catheter navigation. Future work entails effectively steering the robotic catheter using this information. Another important task consists in developing an approach to model vessel bifurcations, where the cylinder model is suboptimal. Lastly, we plan to evaluate the proposed method in more realistic clinical conditions, including physiological processes (e.g. cardiac motion) and catheter navigation in smaller vessels.

REFERENCES

- [1] World Health Organization. (2017) Cardiovascular diseases (cvds). Accessed: 14-09-2020. [Online]. Available: <https://www.who.int/news-room/fact-sheets/detail/cardiovascular-diseases-cvds>
- [2] N. Townsend *et al.*, "Cardiovascular disease in europe: epidemiological update 2016," *European Heart Journal*, vol. 37, no. 42, pp. 3232–3245, 2016.
- [3] H. Rafii-Tari, C. Payne, and G. Yang, "Current and emerging robot-assisted endovascular catheterization technologies: A review," *Annals of Biomedical Engineering*, vol. 42, no. 4, pp. 697–715, 2014.
- [4] J. Bonatti *et al.*, "Robotic technology in cardiovascular medicine," *Nature Reviews Cardiology*, vol. 11, no. 5, pp. 266–275, mar 2014.
- [5] E. Vander Poorten *et al.*, "Cognitive autonomous catheters operating in dynamic environments," *Journal of Medical Robotics Research*, vol. 1, no. 03, p. 1640011, 2016.
- [6] C. Shi *et al.*, "Three-Dimensional Intravascular Reconstruction Techniques Based on Intravascular Ultrasound: A Technical Review," *IEEE Journal of Biomedical and Health Informatics*, vol. 2194, pp. 1–1, 2017.
- [7] C. Shi *et al.*, "Real-time in vitro intravascular reconstruction and navigation for endovascular aortic stent grafting," *The International Journal of Medical Robotics and Computer Assisted Surgery*, vol. 12, no. 4, pp. 648–657, dec 2016.
- [8] C. Bourantas *et al.*, "A new methodology for accurate 3-dimensional coronary artery reconstruction using routine intravascular ultrasound and angiographic data: Implications for widespread assessment of endothelial shear stress in humans," *EuroIntervention*, vol. 9, no. 5, pp. 582–593, 2013.
- [9] A. Karlas and S.-I. Lee, "Towards an IVUS-driven system for endovascular navigation," in *2015 IEEE 12th International Symposium on Biomedical Imaging (ISBI)*. IEEE, apr 2015, pp. 1324–1327.
- [10] C. Gruijthuisen *et al.*, "An automatic registration method for radiation-free catheter navigation guidance," *Journal of Medical Robotics Research*, vol. 1, no. 3, pp. 1–13, 2016.
- [11] C. Shi *et al.*, "Simultaneous catheter and environment modeling for trans-catheter aortic valve implantation," in *2014 IEEE/RSJ International Conference on Intelligent Robots and Systems*, 2014, pp. 2024–2029.
- [12] L. Zhao *et al.*, "Scem+: Real-time robust simultaneous catheter and environment modeling for endovascular navigation," *IEEE Robotics and Automation Letters*, vol. 1, no. 2, pp. 961–968, 2016.
- [13] L. Zhao *et al.*, "Registration-Free Simultaneous Catheter and Environment Modelling," in *MICCAI 2016: 14th International Conference (Vision, Pattern Recognition, and Graphics)*, 2016, pp. 525–533.
- [14] A. Devreker *et al.*, "Fluidic actuation for intra-operative in situ imaging," in *2015 IEEE/RSJ International Conference on Intelligent Robots and Systems (IROS)*, 2015, pp. 1415–1421.
- [15] A. Devreker *et al.*, "Intuitive Control Strategies for Teleoperation of Active Catheters in Endovascular Surgery," *Journal of Medical Robotics Research*, vol. 01, no. 03, p. 1640012, sep 2016.